Numerical Study of the Flow Field Distributor in High-temperature Proton-exchange Membrane Fuel Cells

Xu Han, Pengwei Liu, Shengliang Fan, Yang Liu and Zunlong Jin[*]

School of Mechanical and Power Engineering, Zhengzhou University, Zhengzhou, People's Republic of China
[*]E-mail: zljin@zzu.edu.cn

Uniformity is one of the essential factors for improving the performance of high-temperature proton-exchange membrane fuel cells (HT-PEMFCs). In this study, a new distributor model is established, designed using Murray's law, and the uniformity evaluated in parallel flow fields. The results indicate that the uniformity of oxygen (O_2) distribution in the parallel flow field is directly related to the distributor. Implementing a new distributor, the power density of the cell is increased by 25.2%, uniformity index of O_2 distribution increases by 79.48%, and average pressure drop of the flow field increases by 15.67%. Discussions of theoretical calculations reveal that the average pressure drop was the main factor affecting the uniformity index. Increasing the average pressure drop can improve O_2 consumption and uniformity of O_2 distribution.

1. INTRODUCTION

With the intensification of environmental pollution and energy crises, people have to find some clean and efficient sources of energy [1,2]. Proton-exchange membrane fuel cells (PEMFCs) are clean and efficient energy conversion devices that convert chemical energy from fuels and oxidants directly into water, heat, and electricity via electrochemical reactions [3–5]. Compared with conventional power generators, PEMFCs have been widely studied in recent decades due to their advantages of renewable fuel, high working efficiency, and slight environmental pollution [6].

A typical PEMFC comprises an anode bipolar plate (BP), a membrane electrode assembly (MEA), and a cathode BP, such that BPs are a core component of a PEMFC. Its main functions include (i) supporting the MEA, (ii) providing hydrogen (H_2), oxygen (O_2), and coolant fluid channels and separating H_2 and O_2, (iii) collecting electrons, and (iv) conducting heat. Figuratively speaking, if a fuel cell is regarded as the human body, the BP is equivalent to the bones and blood vessels of the body.

Under normal circumstances, a BP is comprised of a carbon material (e.g., graphite or molded carbon material), a metallic material (e.g., aluminum, nickel, titanium, or stainless steel), and a composite material. There are channels on the BP surface that uniformly distribute the reaction gas, which is called the flow field, to ensure that the reaction gas is uniformity distributed throughout the electrode. Through the design and processing of these channels, the reaction gas can be uniformly distributed to the reaction layer in the MEA for electrochemical reaction.

A flow field with reasonable design can improve flow distribution and enhance cell performance [7–9]. Flow fields can be divided into parallel, serpentine, composite, interdigitated, and bionic flow fields according to their shape. The voltage drop in serpentine and composite flow fields generates higher parasitic power and reduces the cell output power. The generated water in interdigitated flow fields can easily block the gas diffusion layer (GDL) and provide the cell with poor drainage capacity. The manufacturing process of a bionic flow field is complex and difficult to produce on a large scale [10–17]. A parallel flow field has attracted much attention because of its advantages of low parasitic power, good drainage capacity, and simple manufacturing process. However, nonuniform flow distribution is the main defect of parallel flow fields and it is necessary to improve the uniformity of parallel flow fields [1,6,18,19].

Various experiments and simulations have focused on evaluating the uniformity of parallel flow field in fuel cells. For example, Tane [20,21] has conducted a parameterized study of PEMFC through simulation and experimentation and found that increasing pressure and air flow in a channel can improve cell performance and reduce the nonuniformity of generated water in the channel. Zhang et al. [22] have studied the effects of channel cross-section shape on cell performance in parallel flow fields. Zhang et al. [23] have studied two-phase flow in the fuel cell and their results indicated that increasing the flow rate of reaction gas can improve the uniformity of a parallel flow field. Xiao et al. [24] have proposed a calculation method for the uniformity index of gas distribution based on CFD and the results show that increasing the flow rate of inlet gas in a parallel flow field can reduce nonuniformity in the catalytic layer (CL). Lim et al [25] have improved the uniformity of parallel flow fields by changing channel width. In particular, studies regarding the distributor in parallel flow fields have attracted significant attention. Kandlikar et al. [26,27] have designed a new distributor based on pressure drop measurement technology, which is used to manage the distribution of species in the channels. They found that plugging flow in the channel can be effectively suppressed and improve the parallel flow field uniformity after installing the new distributor. Wang et al. [28] have analyzed the momentum of the traditional parallel flow field and designed a new distributor, which improves flow field uniformity and the performance. Maharudrayya et al. [29] have studied distributor structure in a parallel flow field and found that a U-shaped structure offered better uniformity and higher pressure drops in the flow field. However, these studies did not fully examine the relationship between the distributor and uniformity, such that the distributor design process lacks theoretical basis in some studies.

With the development of bionics, many bionic structures have been applied in the field of engineering and have achieved good results. In terms of biological fluids, biologist Cecil Murray has proposed Murray's law based on hydraulic principles followed by human blood circulation. When a fluid flows from a large diameter pipeline to a smaller diameter pipeline, the speed of the fluid increases. This phenomenon will not occur in the human body, because human tissue cannot withstand this pressure. In

the human body, many small blood vessels bifurcate from a large blood vessel and the sum of all small blood vessel cross-sections is greater than that of large blood vessels. Murray's law quantitatively describes this. In an optimal circulation network, the cube of a large blood vessel radius is about equal to the sum of the cube of the small blood vessel radii. For many years, botany textbooks have used condensation theory and plant form pipeline models to explain water transportation in plants. A new study of water flow through the wood of plants shows that Murray's law also applies to plants.

In a parallel flow field, the main function of the distributor is to uniformly distribute fuel and O_2 from the inlet to each reaction channel, which is similar to the blood vessels in the human body. To study whether Murray's law is applicable to the distributor and discuss the effects of distributors on uniformity, this study involved the design of a new distributor according to the Murray's law in biology and established a three-dimensional (3D) HT-PEMFC model coupled with multi-physical fields, including a temperature field. Based on these simulations, several key aspects were discussed, including (i) the effects of the distributor on uniformity of O_2 distribution, pressure drop, and cell performance and (ii) the effects of pressure drop on the uniformity index of O_2 distribution in the flow field.

2. MATHEMATICAL MODEL

2.1. Computational domain

The commercial software COMSOL Multiphysics 5.6 was used to establish a 3D model of the parallel flow field, which consisted of two parts, including electrochemical reaction channels and distributor (Fig. 1b). The distributor consisted of the main channel and subchannels. There were sixteen electrochemical reaction channels in the parallel flow field, with the channels sharing one inlet and one outlet. The overall size of the HT-PEMFC model was $48 \times 58 \times 3.96$ mm^3 (x, y, and z) and the electrochemical reaction area at 48×50 mm^2 (x and y).
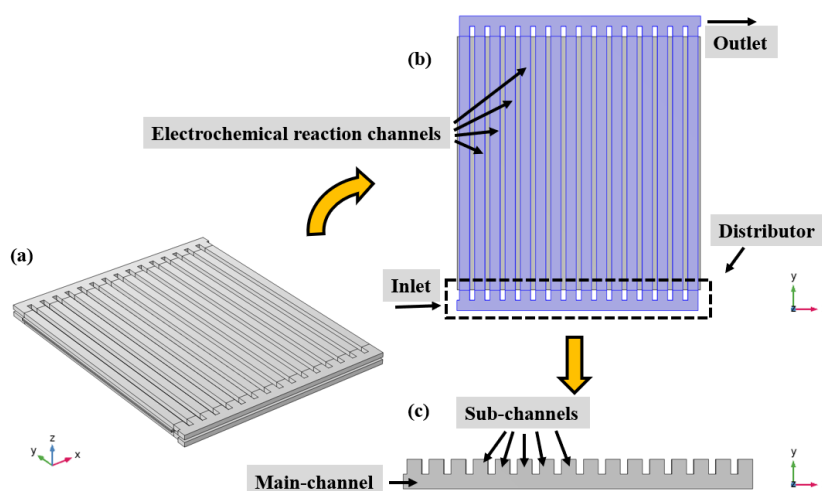
Figure 1. Schematic diagram of the HT-PEMFC model (a), parallel flow field model (*xy* plane, b), and distributor model (c).

The fuel in the anode gas channel was H_2, the oxidizer in the cathode gas channel air, and the electrochemical reaction equations occurring in the fuel cell are shown in Eq. 1, expressed as

$$Cathode: \frac{1}{2}O_2 + 2H^+ + 2e^- \rightarrow H_2O \Bigg\} \quad H_2 + \frac{1}{2}O_2 = H_2O \qquad (1)$$
$$Anode: H_2 \rightarrow 2H^+ + 2e^-$$
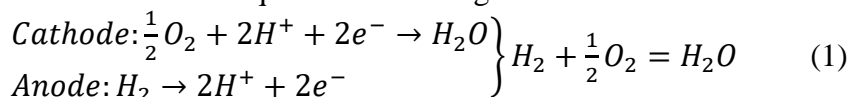
Selected geometric parameters of the model are listed in Table 1.

Table 1. Geometric parameters of the model.

Geometry parameters	Value
Channel length L	5e-2 [m]
Channel width W_{ch}	2e-3 [m]
Channel height H_{ch}	1e-3 [m]
Rib width W_{rib}	1e-3 [m]
BP height H_{BP}	1.5e-3 [m]
GDL thickness H_{GDL}	3.8e-4 [m]
CL thickness H_{CL}	5e-5 [m]
Membrane thickness H_{mem}	1e-4 [m]
Number of channels N	16

2.2. Model assumptions

The working process of the fuel cell was very complex. To simplify the simulation process and minimize the impact on results, the following assumptions were made here:

(1)   The operating state of the model was steady.

(2)   The reaction gas was ideal and incompressible in the channels and the gas flow mode laminar in the channels.

(3)   The material properties of each component in the model were uniform and isotropic.

(4)   The electrochemical reaction only occurred in the CL and the membrane only allowed proton transfer.

2.3. Governing equations

2.3.1. Momentum transfer

In general, momentum transfer mainly includes gas flow in the channels and gas diffusion in the porous media, with channel gas flow expressed by the Navier-Stokes formula and porous media gas diffusion expressed by Darcy's law. However, both equations have limitations in terms of describing the interface between the channel and porous medium. Therefore, a new equation must be introduced to uniformly express momentum transfer involving the channel and porous media; i.e., the Brinkman equation, expressed in Eq. 2 as

$$\rho(\vec{v} \cdot \nabla \vec{v}) = \nabla \left(-pI + \mu \left(\nabla \vec{v} + \left(\nabla \vec{v} \right)^T \right) \right) \qquad (2)$$

The Brinkman equation can uniformly express the momentum transfer of channel and porous media, where ρ is the density, v the velocity, and μ the dynamic viscosity.

2.3.2. Mass transport

The mass transport equation of gas in the channel and porous medium was expressed as Eq. 3

$$\nabla \left(-\rho \cdot w_i \sum_{j=1}^{N} D_{ij} \left(\frac{M}{M_j} \left(\nabla w_j + w_j \frac{\nabla M}{M} \right) + \left(x_j - w_j \right) \frac{\nabla P}{P} \right) + w_j \cdot \rho \cdot \vec{v} \right) = S_i \quad (3)$$

where w is the molar fraction, D the binary diffusion coefficient, M the molar mass, and S the source term.

The computational equation of dynamic viscosity and diffusion coefficient of various reaction gases are listed in Table 2 [30], with temperature the main influencing factor of these parameters. Moreover, the dynamic viscosity and density of mixed gases also need to consider their mole fraction, shown in Eqs. 4 and 5 as

$$\mu_{an/ca} = \sum_{i=1}^{n} \frac{w_i \mu_i}{\sum_{j=1}^{n} \left(w_j \sqrt{\frac{M_j}{M_i}} \right)} \quad (4)$$

$$\rho = P \left(RT \sum_i \frac{w_i}{M_i} \right)^{-1} \quad (5)$$

The velocity equations of the anode and cathode were expressed as

$$U_{in\_an} = \lambda_{an} \frac{1}{2F} w_{H_2} \frac{RT}{p \cdot A_{ch}} \quad (6)$$

$$U_{in\_ca} = \lambda_{ca} \frac{1}{4F} w_{O_2} \frac{RT}{p \cdot A_{ch}} \quad (7)$$

where λ is the stoichiometry, R and T the universal gas constant and temperature, respectively, and A_{ch} the channel area.

Table 2. Dynamic viscosity equations and diffusion coefficient equations

Mass transport parameters	Value
Dynamic viscosity of H$_2$ μ_{H2}	27.76e-7+2.12e-8·T-3.28e-12·T^2 [Pa*s]
Dynamic viscosity of O$_2$ μ_{O2}	44.22e-7+5.62e-8·T-1.13e-12·T^2 [Pa*s]
Dynamic viscosity of nitrogen μ_{N2}	42.61e-7+4.75e-8·T-9.88e-12·T^2 [Pa*s]
Dynamic viscosity of water μ_{H2O}	-36.83e-7+4.29e-8·T-1.62e-12·T^2 [Pa*s]
Diffusion coefficient $D_{H2\text{-}H2O}$	9.15e-5· (T/307.1)$^{1.75}$ [m^2/s]
Diffusion coefficient $D_{O2\text{-}H2O}$	2.82e-5· (T/308.1)$^{1.75}$ [m^2/s]
Diffusion coefficient $D_{N2\text{-}H2O}$	2.56e-5· (T/307.1)$^{1.75}$ [m^2/s]
Diffusion coefficient $D_{O2\text{-}N2}$	2.2e-5· (T/293.2)$^{1.75}$ [m^2/s]

2.3.3. Heat transfer

Heat transfer of a fuel cell is based on the theory of local thermal equilibrium (LTE), which requires consideration of heat generation, transfer, and consumption. The energy conservation equation in the heat transfer process was

$$\nabla \cdot \left(\rho C_p \vec{v} T\right) = \nabla \cdot (k \nabla T) + Q_{total} \qquad (8)$$

where C_p is the heat capacity, k the thermal conductivity, and Q_{total} the heat source. The equations for heat capacity and thermal conductivity of multispecies were

$$C_p = \sum_i w_i C_{p\_i} \qquad (9)$$

$$k = \sum_i w_i k_i \qquad (10)$$

The total heat source of the fuel cell comprised three sources, including electrochemical reaction heat Q_{react}, ohmic polarization heat Q_{ohmic}, and activation polarization heat $Q_{activation}$, and shown in Eq. 11 as

$$Q_{total} = Q_{react} + Q_{ohmic} + Q_{activation} \qquad (11)$$

The equations of each heat source are

$$Q_{react\_an/ca} = \left(-T\Delta S_{an/ca}\right) \cdot \frac{i}{nF} \qquad (12)$$

$$Q_{ohmic} = \|\nabla \phi_{ele}\|^2 \cdot \sigma_{ele}^{eff} + \|\nabla \phi_{pro}\|^2 \cdot \sigma_{pro}^{eff} \qquad (13)$$

$$Q_{activation\_an/ca} = i_{an/ca} |\eta_{act\_an/ca}| \qquad (14)$$

where ΔS is the entropy increase, n the number of electrons transferred, F the Faraday constant, ϕ and σ the electric potential and conductivity (electronic and proton), respectively, i the current density, and η_{act} the activation loss.

2.3.4. Electrochemistry

The calculation method of electrode dynamics in the fuel cell used the Butler-Volmer equations [3]. The equations of volume exchange current density at the anode and cathode were expressed as

$$i_{an} = A_V \cdot i_{0,ref\_an} \left(\frac{c_{H_2}}{c_{H_2,ref}}\right)^{0.5} \left(exp\left(\frac{n\alpha_{an}}{RT}F\eta_{act\_an}\right) - exp\left(\frac{-n\alpha_{ca}}{RT}F\eta_{act\_an}\right)\right) \qquad (15)$$

$$i_{ca} = A_V \cdot i_{0,ref\_ca} \left(\frac{c_{O_2}}{c_{O_2,ref}}\right)^{1} \left(-exp\left(\frac{n\alpha_{an}}{RT}F\eta_{act\_ca}\right) + exp\left(\frac{-n\alpha_{ca}}{RT}F\eta_{act\_ca}\right)\right) \qquad (16)$$

where A_V is the activation specific surface area, $i_{0,ref}$ the reference exchange current density, c the gas concentration, and α the transfer coefficient.

The equations of reference exchange current density at anode and cathode were

$$i_{0,ref\_an} = 7.135\, exp\left(-1400(1/T - 1/353.15)\right) \qquad (17)$$

$$i_{0,ref\_ca} = 1.2286e - 6\, exp\left(-7900(1/T - 1/353.15)\right) \qquad (18)$$

The equations of activation loss at anode and cathode were

$$\eta_{an} = \left(\phi_{ele\_an} - \phi_{pro\_an}\right) - E_{eq\_an} \qquad (19)$$

$$\eta_{ca} = \left(\phi_{ele\_ca} - \phi_{pro\_ca}\right) - E_{eq\_ca} \qquad (20)$$

where $\phi_{ele;pro}$ is the electric potential (electronic and proton) and E_{eq} the equilibrium electric potential.

The equations of equilibrium electric potential at the anode and cathode were

$$E_{eq\_an} = \frac{RT}{2F} \ln \frac{p_{H_2O}}{p_{H_2}} \qquad (21)$$

$$E_{eq\_ca} = E_0 + \frac{RT}{4F} \ln \frac{p_{O_2}}{P_0} \qquad (22)$$

where p_i is the species pressure, p_0 the standard atmospheric pressure, and E_0 the open circuit voltage.

Selected material and electrochemistry parameters of the model are listed in Table 3.

Table 3. Material parameters and electrochemistry parameters of the model.

Parameters	Value
GDL permeability κ_{GDL}	1.18e-11[m^2]
CL permeability κ_{CL}	2.36e-12[m^2]
GDL porosity ε_{GDL}	40%
CL porosity ε_{CL}	40%
Electrolyte electric conductivity σ_0	9.85[S/m]
Electrode conductivity σ_s	222[S/m]
Anode stoichiometry number λ_{an}	1.2
Cathode stoichiometry number λ_{ca}	2.0
Anode charge transfer coefficient α_{an}	0.5
Cathode charge transfer coefficient α_{ca}	0.25
Activation specific surface area A_V	1e7[m^2/m^3]

2.4. Boundary conditions

The following boundary conditions and assumptions were implemented in the established model:

(1) For gas channels of the anode and cathode, the temperature, flow rate, and species of the gas at the inlet boundary were constant and the gas humidified at 28°C to 100% relative humidity.

Table 4. Boundary parameters of the model.

Boundary parameters	Value
Cell temperature T	180+273.15 [K]
Reference pressure P_{ref}	1 [atm]
Water partial pressure P_{H2O}	4781.4 [Pa]
Relative humidity, anode inlet RH_{an}	100%
Relative humidity, cathode inlet RH_{ca}	100%
Water inlet molar fraction, anode and cathode w_{H2O}	0.037319
Inlet O_2 molar fraction w_{O2}	0.20216
Inlet N_2 molar fraction w_{N2}	0.76502
Inlet H_2 molar fraction w_{H2}	0.96268

(2) The pressure of the outlet boundary was standard atmospheric pressure and there was no surface slip at the inface at the channel wall.

(3) The anode and cathode BPs had a ground surface and voltage loading surface, respectively, and there was no contact resistance at the interface with the GDL (i.e., the assembly pressure was not considered).

(4) Generated heat was only dislodged by the gas channel and not through the BPs, which comprised heat-insulating materials.

Selected boundary parameters of the model are listed in Table 4.

2.5. Numerical algorithm and method

The model used in this study was constructed using the business software COMSOL Multiphysics 5.6, including a finite volume computational method and the following physical fields: proton exchange, free and porous media flow, and porous media heat transfer. The parameters of the solver were as follows: a steady-state solver in a solver configuration; the linear solver of potential variables, H_2 mixtures, O_2 mixtures, and temperature, as PALDISO; the linear solver of speed and pressure, as GMRES; the maximum number of iterations was 150; and the relative tolerance at 10^{-4}. A parametric sweep was performed before the calculations, where the parameter was the cell voltage, and the sweep method involved gradually reducing the voltage from 0.9 to 0.3 V with a step size of -0.1 V.

3. MODEL VALIDATION

To verify the simulation result, the model was tested at 180°C, 1 atm back pressure, and anode and cathode stoichiometry at 1.2 and 2, respectively, and the results compared with experimental data collected from the literature [31]. Comparison of the obtained polarization curves were based on simulation results and experimental data, where the right y-axis was the voltage deviation (Fig. 2a). The maximum deviation was 1.2%, which was within a reasonable range and indicated that the simulation results were consistent with the experimental data. There were many potential reasons for the observed deviation, including experimental measurement and simulation parameter error. The parameter error arose from the fact that some parameters of the model were not obtained directly through measurements, but rather, they were only approximated to experimental values by adjusting the coefficients in the model equations (e.g., reference exchange current density and activation specific surface area).

The current density and calculation time of the model using different mesh numbers at the same operating voltage (0.5 V) is shown in Figure 2b. The model was meshed six times, with the following mesh numbers: 109860, 159818, 196337, 244973, and 306188. According to Figure 2b, the current density changed significantly when the mesh number increased from 109860 to 196337, although it stabilized when the mesh number was >196337. Considering the principle that "the less calculation time (without sacrificing model performance), the better," it was decided to use the model with a mesh number of 196337.

(a)

(b)
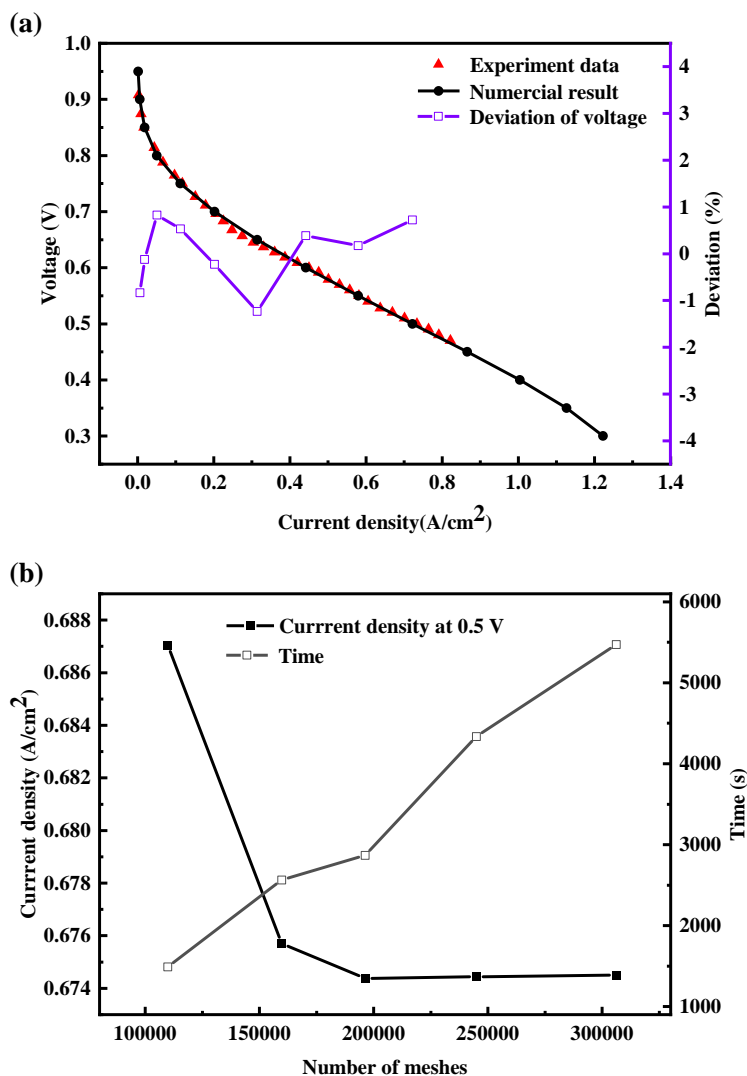
Figure 2. Model validation: comparison of polarization curves from simulations and experimental data (a) and current density and calculation time as a function of mesh numbers at 0.5 V (b).

4. RESULTS AND DISCUSSION

In a parallel flow field, the main function of the distributor is to uniformly distribute the fuel and O_2 from the inlet to each reaction channel and, therefore, a reasonable distributor can improve the uniformity of the flow field. Four different distributor models were established in this study (Fig. 3). Case 1 was a traditional distributor model, with its main channel width equal to the width of the electrochemical reaction channel W_{ch}. Cases 2 and 3 were distributor models with a broadened main channel, with the main channel W_{ch} width doubled and tripled, respectively. Case 4 was a new distributor model, with its main channel designed using Murray's law.

Case 1

Case 2

Case 3

Case 4
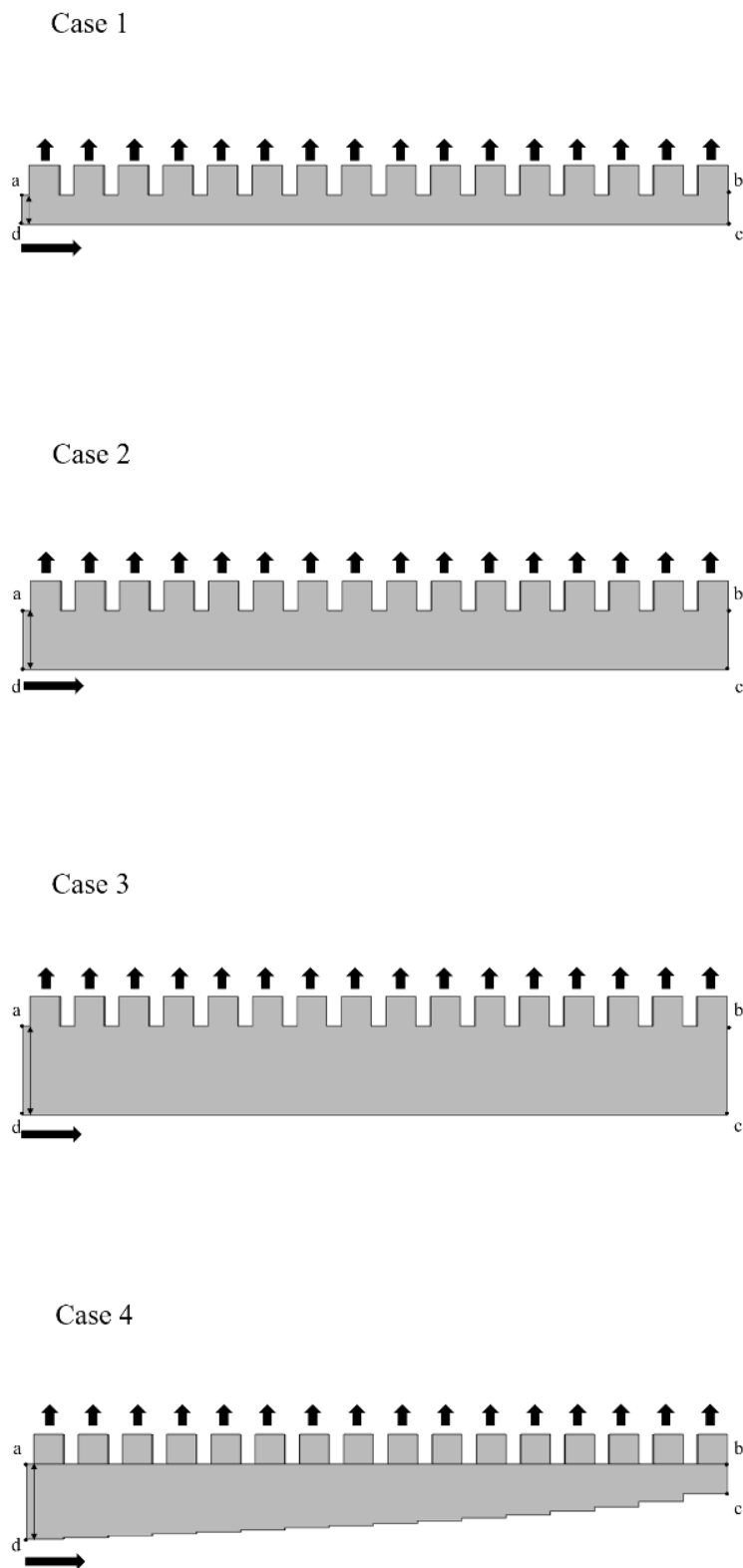
Figure 3. Schematic diagrams of the four distributor models.

4.1. Oxygen distribution

4.1.1. Mass flow rate of O_2

In the parallel flow field, the O_2 of the cathode flows into each reaction channel after passing through the distributor, such that the distributor directly affects O_2 distribution in the reaction channel. In this study, the O_2 mass flow at the entrance and exit of each reaction channel was separately collected and the O_2 consumption calculated. O_2 consumption here refers to the difference between the O_2 mass flow at the channel entrance and exit. The mass flow rate of O_2 at entrances and exits was $\dot{m}_{O_2}$ and the coordinate the distance between the center of the reaction channel entrance and distributor inlet (Fig. 4).

In the parallel flow field, the O_2 mass flow rate curves of reaction-channel entrances and exits were all concave (Figs. 4a and 4b). The O_2 mass flow rate of the reaction channels located in the middle coordinates (*x*-axis) were low, while the O_2 mass flow rate of the reaction channels near the main-channel exit (coordinate, 46.5 mm) were higher. Among them, the traditional distributor (Case 1) had the largest change range, with a maximum $\dot{m}_{O_2}$ at the entrance of 7.24×10^{-7} kg/s, which was 24.0% higher than the minimum (5.84×10^{-7} kg/s). The maximum of $\dot{m}_{O_2}$ at the exit was 3.5×10^{-7} kg/s, which was 64.3% higher than the minimum (2.13×10^{-7} kg/s). With increased main-channel width (Case 2 and Case 3), the O_2 mass flow rate curves gradually flattened and the O_2 flow in the reaction channels gradually became uniform. However, the new distributor (Case 4) had the smallest change range, the smoothest O_2 mass flow rate curve, and the O_2 flow in the reaction channels the most uniform. When using the new distributor, the deviation between the maximum and minimum of $\dot{m}_{O_2}$ at the entrance and exit of the reaction channels were only 7.5 and 18.4%, respectively.

Observations of the O_2 consumption in each reaction channel showed that, among them, the O_2 consumption curve of Case 1 was the most tortuous and the difference between the O_2 consumptions of each reaction channel the largest (Fig. 4c). The maximum O_2 consumption in all reaction channels was 4.19×10^{-7} kg/s and the minimum value at 3.71×10^{-7} kg/s, with a difference of 12.9%. This meant that the traditional distributor led to uneven O_2 consumption in the parallel flow field. With increased main channel width, the O_2 consumption curves gradually flattened. However, the O_2 consumption curve of Case 4 was the smoothest and the deviation between the maximum and minimum of O_2 consumption only 2.3%, which meant that the uniformity of O_2 consumption in parallel flow fields can be improved using the new distributor.

(a)

(b)

(c)
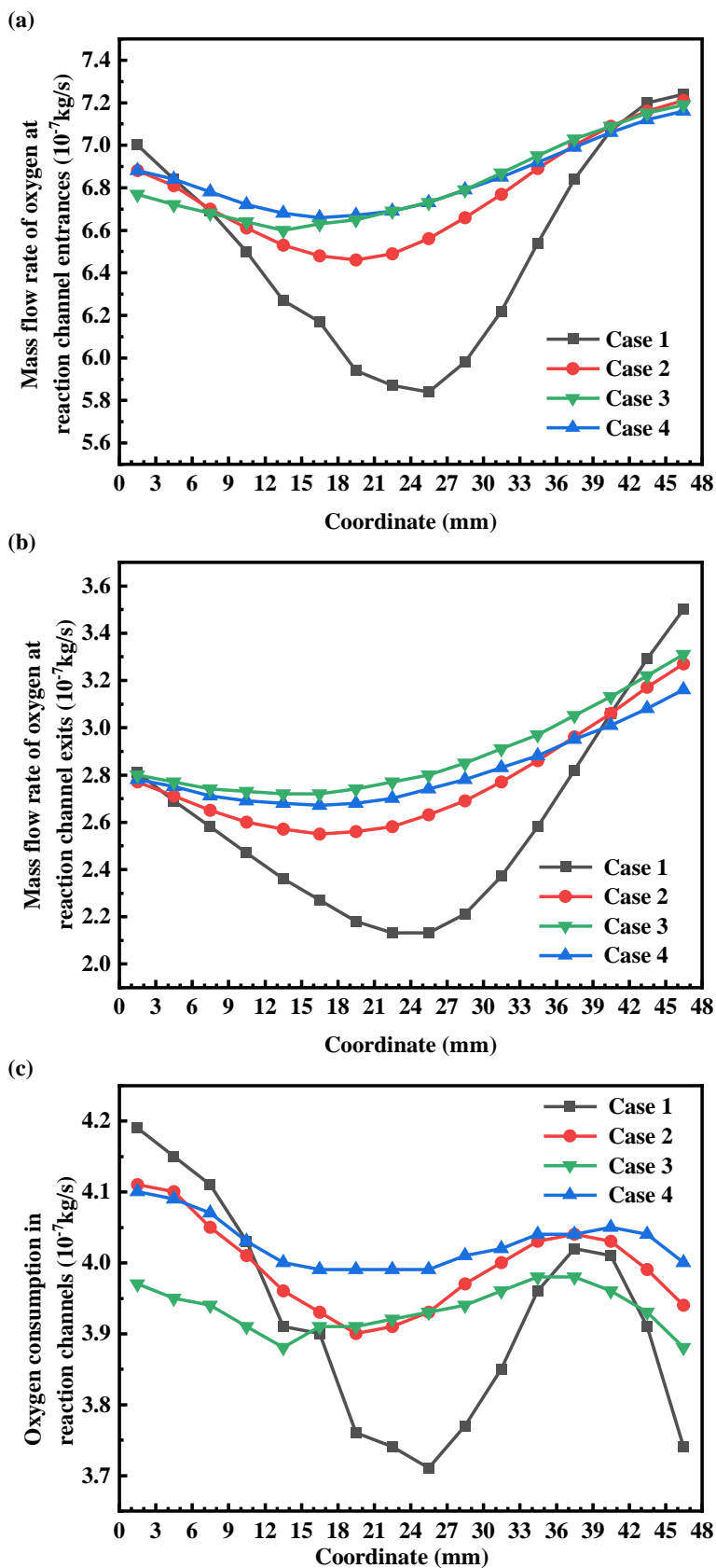
Figure 4. The mass flow rate of O_2 $\dot{m}_{O_2}$ at entrances (a) and exits (b) and O_2 consumption (c) in reaction channels at 0.5 V.

4.1.2. Oxygen concentration

Uniformity is one of the important factors affecting electrochemical reactions. Uniformly-distributed reaction gases will improve the reaction efficiency of catalysts and increase the effective reaction area of the catalytic layer [32]. The O_2 molar concentration at the interface between the cathode CL and GDL was considered (Fig. 5). In these four cases, the O_2 molar concentration gradually decreased along the flow direction (*y*-axis). The diffusion rate and consumption rate of O_2 are two important factors affecting the O_2 concentration in the CL. When O_2 entered the reaction channel from the distributor, the diffusion rate was greater than the consumption rate, such that the O_2 concentration in the first half of the CL was the highest. Also, high temperature promoted the O_2 reduction reaction (ORR) to consume more O_2 in the second half of the CL, with the consumption rate faster than the diffusion rate. Thus, the O_2 concentration of the CL gradually decreased along the *y*-axis direction.
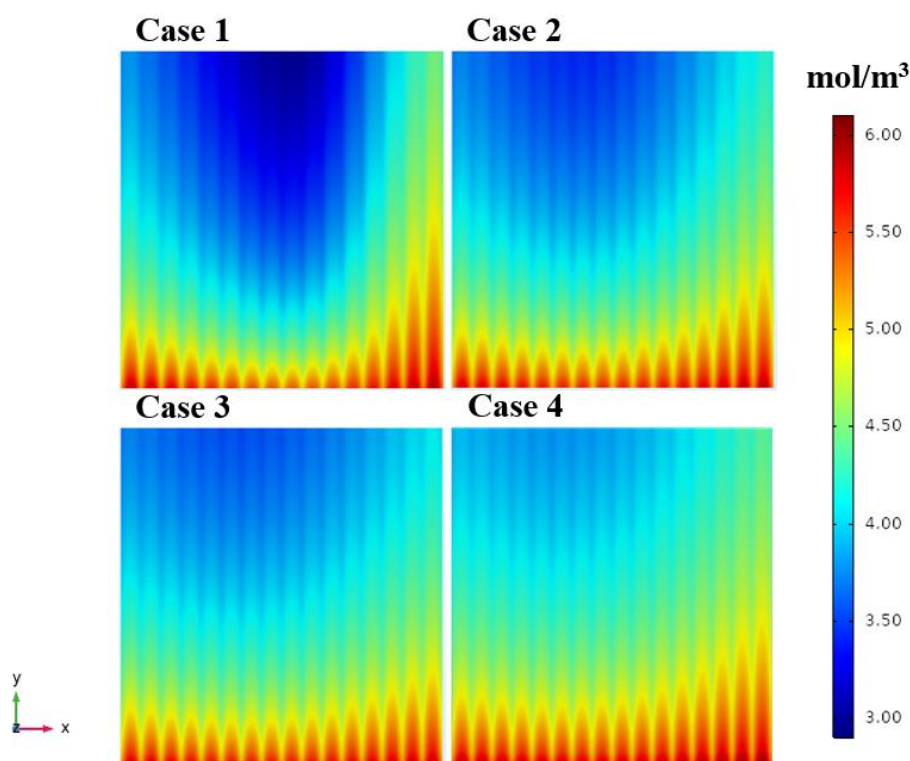
Figure 5. O_2 molar concentration at the interface between the cathode CL and GDL of four cases.

However, the low O_2 concentration area (Fig. 5, blue area) of the CL in Case 1 was found to be the highest, which was caused by the uneven distribution of O_2 by the traditional distributor. In the central area of the CL, the diffusion rate of O_2 due to insufficient O_2 supply was very small, which was far lower than the consumption rate of electrochemical reactions in this area. Therefore, there was a large area of low O_2 concentration in this area. In both side areas of the CL, the O_2 supply was thus sufficient and the diffusion rate greater than the consumption rate. Therefore, the O_2 concentration was relatively high in this area. The larger the area of the low O_2 concentration was, the lower the O_2 utilization rate in

the CL, resulting in a shortage of O_2 in some areas and excess O_2 in some areas. This reduced the effective electrochemical reaction area in the CL and affected the cell output power. Compared with Cases 1, 2, and 3, it was found that increasing the main channel width of the distributor improved the uniformity of O_2 concentration distribution in the CL. However, observation of Case 4 found that use of the new distributor not only improved the uniformity of O_2 distribution, but also improved the O_2 concentration of the CL. Uniform and sufficient O_2 helped electrochemical reactions and improved cell output power.

4.2. Pressure drop distribution

In the parallel flow field, sufficient and uniform O_2 in the channel was conducive to improving the diffusion rate of O_2 flow to CL and the uniformity of O_2 distribution in CL. In the reaction channel, pressure drop directly affected the flow and distribution of O_2 [28,33,34], such that it was necessary to examine the pressure drop in the flow field. The pressure drop curves of the four cases at 0.5 V showed that, in the parallel flow field, the curves were all concave (Fig. 6a). The pressure drops located in the middle coordinates (*x*-axis) were low, while pressure drops near the main-channel exit (coordinate, 46.5 mm) were the highest. Among these, the traditional distributor (Case 1) had the largest range of change, with the maximum pressure drop at 173 Pa, which was ~12-fold higher than the minimum (14 Pa). With increased main-channel width (Cases 2 and 3), pressure drop curves gradually flattened and the pressure drop in reaction channels gradually became uniform. However, the new distributor (Case 4) had the smallest range of change, the smoothest pressure drop curve, and the pressure drop in reaction channels most uniform. When using the new distributor, the deviation between the maximum and minimum pressure drop was only ~1-fold.

The nonuniformity and average pressure drops for the four cases at 0.5 V indicated that the larger the standard deviation of pressure drop, the more nonuniformity the pressure distribution was (Fig. 6b). Case 1 exhibited the highest standard deviation, at 4.04, which meant that the traditional distributor caused a nonuniform pressure drop distribution in the flow field. With increased width of the main channel (Cases 2 and 3), the standard deviation of pressure drop gradually decreased and the pressure drop distribution gradually became uniform in the flow field. However, the standard deviation of Case 4 was only 1.19, which was the lowest of all cases. This meant that the new distributor reduced the standard deviation by ~70.5% and effectively improved the uniformity of pressure drop in the flow field. Case 1 had the lowest average of pressure drop, at 42.31 Pa, and Case 4 the highest average pressure drop, at 48.94 Pa. This meant that, compared with the traditional distributor, the new distributor increased the average pressure drop by ~15.7%. In the parallel flow field, the pressure drop in the channel had a direct effect on the O_2 flow, with the greater the pressure drop was, the higher the $\dot{m}_{O_2}$ [6].

Under the same initial conditions, the pressure drop of the serpentine flow field is higher than that of the parallel flow field [35]. In the reaction channel, pressure drop forces more O_2 to enter the CL to participate in electrochemical reactions, such that the serpentine flow field outputs higher current. However, excessive pressure drop will cause the fuel cell to generate huge parasitic power and reduce the comprehensive cell performance [36]. Therefore, appropriately increasing the pressure drop in the

flow field can improve cell performance. In this study, the new distributor improved the average pressure drop in the reaction channel and was at the same order of magnitude as the traditional distributor, such that additional parasitic power generated was ignored.
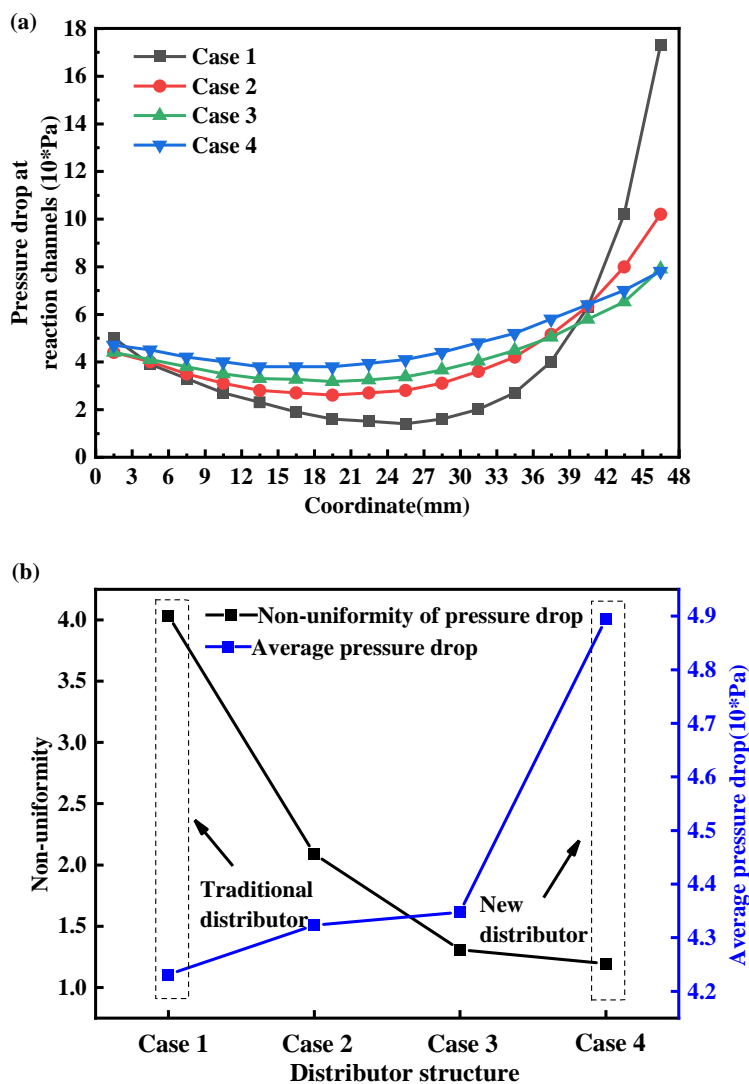
Figure 6. Pressure drop distribution of four cases. Pressure drop curves (a) and nonuniformity (left) and average (right) of pressure drop (b).

4.3. Determination coefficient

The structure of the distributor had a direct impact on the pressure drop in the flow field. According to a previous study on pressure drop in the flow channel and the mass flow rate of the gas [6], it was seen here that the equation of the gas mass flow rate and channel pressure drop channel could be expressed as Eq. 23

$$\dot{m} = \left(\frac{1}{Re\,f} \frac{D_c^2 A_c}{2L_c} \frac{\rho}{\mu} \right) \Delta P = K \Delta P \qquad (23)$$

where the $\dot{m}$ is the gas mass flow rate; Ref a fixed value; D_c, A_c, and L_c the hydraulic diameter, cross-sectional area, and channel length, respectively; ρ and μ the gas density and gas viscosity, respectively; and ΔP and K the pressure drop and coefficient, respectively. The equation shows that the mass flow rate of gas in the channel is directly proportional to the pressure drop.

The equation of $\dot{m}$ and ΔP in each reaction channel was expressed as Eq. 24

$$\dot{m}_i = K\Delta P_i \qquad (24)$$

Therefore, the average mass flow rate in N channels was

$$\overline{\dot{m}} = \frac{1}{N}\sum_{i=1}^{N}\dot{m}_i = \frac{1}{N}\sum_{i=1}^{N}K\Delta P_i = K\Delta\overline{P} \qquad (25)$$

where the $\Delta\overline{P}$ is the average pressure drop.

At the entrance of the main channel, the total of mass flow rate was constant and expressed as

$$K = \frac{\overline{\dot{m}}}{\Delta\overline{P}} = \frac{\dot{m}_{total}}{N\Delta\overline{P}} \qquad (26)$$

where the $\dot{m}_{total}$ is the total of mass flow rate in all channels.

In this study, the standard deviation was used to indicate the nonuniformity of the mass flow rate and expressed as

$$D_{\dot{m}} = \sqrt{\frac{\sum_{i=1}^{N}\left(\dot{m}_i - \overline{\dot{m}}\right)^2}{N}} \qquad (27)$$

$$D_{\Delta P} = \sqrt{\frac{\sum_{i=1}^{N}\left(\Delta P_i - \Delta\overline{P}\right)^2}{N}} \qquad (28)$$

Substituting Eqs. 25, 26, and 28 into Eq. 27, $D_{\dot{m}}$ in Eq. 29 was expressed as

$$D_{\dot{m}} = \frac{\dot{m}_{total}}{N} \cdot \frac{D_{\Delta P}}{\Delta\overline{P}} \qquad (29)$$

where the $\dot{m}_{total}$ and N (the number of channels) are constant. Therefore, the factors affecting the nonuniformity of mass flow were the standard deviation of the pressure drop $D_{\Delta P}$ and $\Delta\overline{P}$. Eq. 29 showed that $D_{\dot{m}}$ was directly proportional to $D_{\Delta P}$ and inversely proportional to the $\Delta\overline{P}$. This meant that there were two ways to reduce the nonuniformity of the mass flow rate. One was to reduce the nonuniformity of pressure drop and the other was to increase the average pressure drop. Between these two ways, the second one (increased average pressure drop) was simple and practical.

Under the same initial conditions (total mass flow rate and number of channels constant), the two factors affecting the nonuniformity of mass flow rate were the nonuniformity of pressure drop and average pressure drop. To study the impact of these two factors on the nonuniformity of mass flow rate, the statistical determination coefficient of linear fitting R^2 was employed. Among these, the independent variable was the reciprocal of average pressure drop $\frac{1}{\Delta\overline{P}}$, and the dependent variable the standard deviation (nonuniformity) of the mass flow rate $D_{\dot{m}}$. The average pressure-drop and mass flow rates of Case 4 at different voltages were examined here, with ten sets of data ($\frac{1}{\Delta\overline{P}}$ and $D_{\dot{m}}$) collected, and the determination coefficient R^2 calculated by linear fitting. Unexpectedly, the results showed that the determination coefficient R^2 was 0.997 (Fig. 7). This meant that the average pressure drop had an absolute effect on the standard deviation of the mass flow rate, while the standard deviation of the pressure drop had little effect on the standard deviation of the mass flow rate. Therefore, the new distributor reduced the standard deviation of the mass flow rate and improved the uniformity of O_2 distribution by increasing the average pressure drop in the flow field.
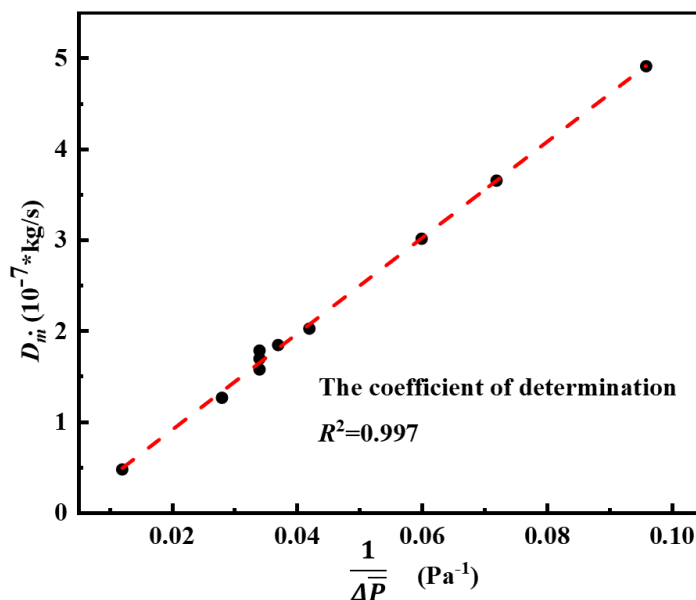
Figure 7. Linear fitting of the reciprocal of average pressure drop $\frac{1}{\overline{\Delta P}}$ and the standard deviation of mass flow rate $D_{\dot{m}}$.

4.4. Cell performance

Considering O_2 molar concentration, standard deviation of mass flow rate, standard deviation of pressure drop, and average pressure drop confirmed that the average pressure drop was the dominant factor affecting O_2 distribution uniformity, whereas the standard deviation of the pressure drop was an ignorable factor. In terms of overall cell performance, the effects of the new distributor were consistent with the previous discussion.

Polarization and power density curves of the four cases showed that current density in each case increased as voltage decreased (Figs. 8a and 8b). Specifically, when the voltage was between 0.9–0.8 V, current density curves of all cases essentially coincided. As voltage continued to drop from 0.8 V, differences between the current density curves of the four cases gradually emerged. When the voltage decreased to 0.3 V, the current densities of all cases reached their maxima.

At a cell voltage of 0.3 V, the current densities of Cases 1, 2, and 3 were 1.789, 1.879, and 1.904 A/cm^2, respectively. Increasing the width of the main channel can increase the average pressure drop in the flow field, according to the discussion in Section 4.2, and the Case 3 current density the highest. Comparing current densities of Cases 1, 3, and 4 revealed that the current density of Case 4 (2.274 A/cm^2) was the highest in all cases, at ~27.1%, and 16.3% higher than Cases 1 and 3, respectively. This showed that, in terms of cell performance improvement, it was better to use a distributor designed with Murray's law than to increase the main-channel width and the new distributor improved fuel cell performance. Due to the average pressure drop of the flow field being inversely proportional to the standard deviation (nonuniformity) of O_2 mass flow rate, the larger the average pressure drop was, the more uniform the O_2 distribution. The new distributor improves the uniformity of O_2 mass flow by increasing the average pressure drop. The O_2 consumption in reaction channels can be increased and the

area of low O_2 concentration in cathode CL can be reduced using the new distributor. Sufficient and uniform O_2 helps to improve the electrochemical reactions and the cell performance. Therefore, cell current density with the new distributor was higher at the same voltage.

An analogous conclusion was drawn based on the power density curves (Fig 8b); i.e., cell output power with the new distributor was the highest. For this reason, the new distributor designed with Murray's law in this study can provide an option for fuel cell flow field optimization.
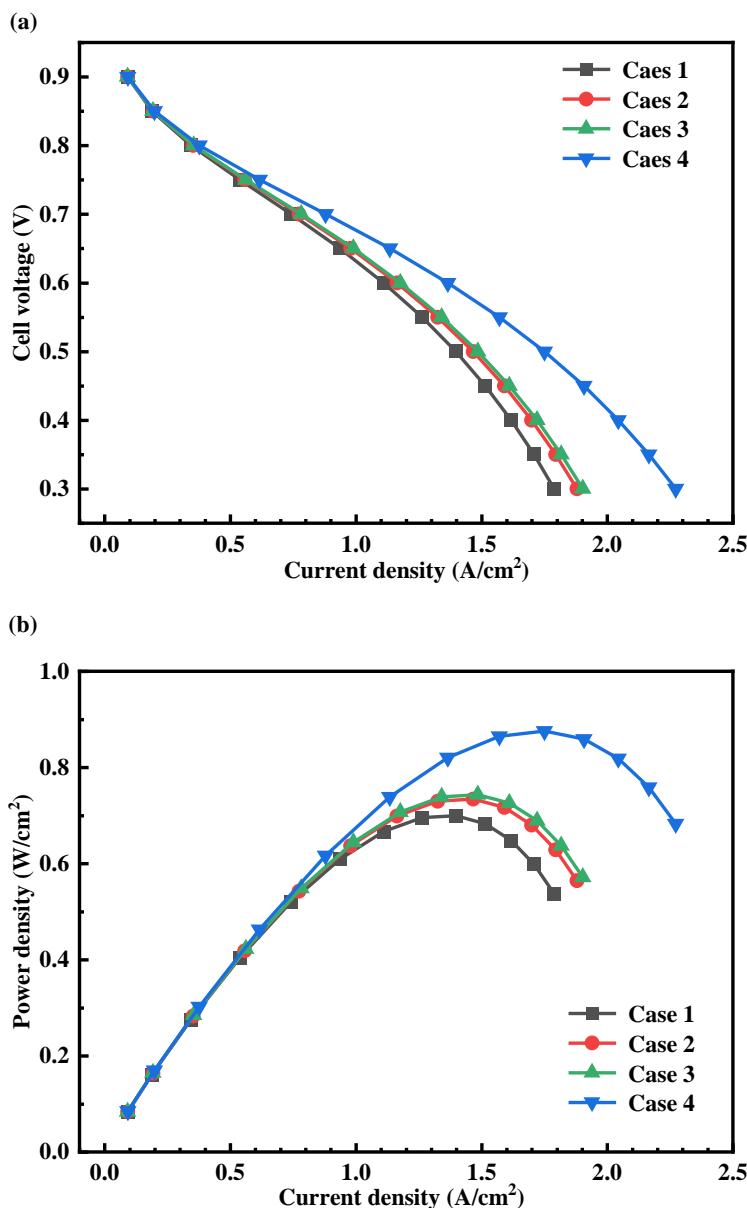
Figure 8. Cell performance for each of the four evaluated cases: polarization curves (a) and power density curves (b).

5. CONCLUSIONS

In this study, four different distributor models were established, including a new distributor designed with Murray's law to evaluate the effects of the distributor on O_2 mass flow rate, O_2 concentration, average pressure drop of the flow field, and cell performance. The main conclusions drawn from the results were as follows: (i) The new distributor improved the uniformity of O_2 distribution in the cathode flow field and increased the O_2 consumption. (ii) In the flow field with the new distributor, the average pressure drop increased by 15.7% and the uniformity of the pressure drop distribution increased by 70.5%. (iii) In terms of cell performance, the new distributor increased the current density by 27.1 (0.3 V) and peak power density by 25.2%.

By analyzing the equation of pressure drop and mass flow rate, it was found that, under the same initial conditions, the two factors affecting nonuniformity of mass flow rate were the nonuniformity of pressure drop and average pressure drop. The determination coefficient R^2 was 0.997 of the $\frac{1}{\overline{\Delta P}}$, and the $D_{\dot{m}}$ calculated by linear fitting. This indicated that the average pressure drop had an absolute effect on the standard deviation of mass flow rate, while the standard deviation of pressure drop had little effect on the standard deviation of mass flow rate. In fuel cells, the uniformity of O_2 distribution and cell performance was improved by increasing the average pressure drop of the flow field, such as serpentine flow field. However, the average pressure drop at the new and traditional distributors were in the same order of magnitude, such that additional generated parasitic power could be ignored.

Overall, this was a feasible and effective method for using and examining this new distributor designed with Murray's law for improving the uniformity of O_2 distribution. As in other fields, there have been many cases of the application of bionic structure in fuel cells, which are gradually being called mainstream. The results of the new distributor only represent the tip of the iceberg and the study on the optimization of the flow field structure in fuel cells requires more attention.

DATE AVAILABILITY
The data that support the findings of this study are available from the corresponding author upon reasonable request.

References

1.   F. Martins, C. Felgueiras, M. Smitkova and N. Caetano, *Energies*, 12 (2019) 964.
2.   X.D. Wang, Y.Y. Duan, W.M. Yan and X.F. Peng, *Electrochim. Acta*, 53 (2008) 5334.
3.   P. Liu, S. Fan, Y. Liu, X. Han and Z. Jin, *J. Electrochem. Soc.*, 168 (2021) 104501.
4.   S. Fan, J. Ye, Q. Yao, D. Wang, L. Yang and Z. Jin, *Int. J. Energy Res.* 46 (2021) 176.
5.   Y. Vazifeshenas, K. Sedighi and M. Shakeri, *Int. J. Hydrogen Energy*, 40 (2015) 15032.
6.   R.J. Kee, P. Korada, K. Walters and M. Pavol, *J. Power Sources*, 109 (2002) 148.
7.   D.H. Ahmed and H.J. Sung, *J. Power Sources*, 162 (2006) 327.
8.   L.J. Yu, G.P. Ren, M.J. Qin and X.M. Jiang, *Renew. Energy*, 34 (2009) 530.

9. W.J. Yang, S.J. Kang and Y.B. Kim, *Int. J. Energy Res.*, 36 (2012) 1051.
10. K.S. Choi, H.M. Kim and S.M. Moon, *Int. J. Hydrogen Energy*, 36 (2011) 1613.
11. A. Iranzo, P. Boillat, J. Biesdorf, E. Tapia, A. Salva and J. Guerra, *Int. J. Hydrogen Energy*, 39 (2014) 15687.
12. M. Mehrpooya, M. Kheir Rouz and A. Nikfarjam, *Ind. Eng. Chem. Res.*, 54 (2015) 3640.
13. N.J. Cooper, A.D. Santamaria, M.K. Becton and J.W. Park, *Energy Convers. Manag.*, 136 (2017) 307.
14. Q.F. Jian, G.Q. Ma and X.L. Qiu, *Renew. Energy*, 62 (2014) 129.
15. A.D. Santamaria, N.J. Cooper, M.K. Becton and J.W. Park, *Int. J. Hydrogen Energy*, 38 (2013) 16253.
16. P.V. Suresh and S. Jayanti, *Environ. Sci. Pollut. Res.*, 23 (2016) 27074933.
17. S.S. Hsieh, B.S. Her and Y.J. Huang, *Energy Convers. Manag.*, 52 (2011) 975.
18. T. Wilberforce, Z. El Hassan, E. Ogungbemi, O. Ijaodola, F.N. Khatib, A. Durrant, J. Thompson, A. Baroutaji and A.G. Olabi, *Renew. Sustain. Energy Rev.*, 111 (2019) 236.
19. R. Anderson, L. Zhang, Y. Ding, M. Blanco, X. Bi and D.P. Wilkinson, *J. Power Sources*, 195 (2010) 4531.
20. T. Taner, *Energy*, 143 (2018) 284.
21. T. Taner, *J. Therm. Eng.*, 3 (2017) 1515.
22. W. Zhang, P. Hu, X. Lai and L. Peng, *J. Power Sources*, 194 (2009) 931.
23. L. Zhang, H.T. Bi, D.P. Wilkinson, J. Stumper and H. Wang, *J. Power Sources*, 183 (2008) 643.
24. Y. Xiao, P. Ming, M. Hou, Y. Fu, B. Yi and Z.G. Shao, *J. Power Sources*, 185 (2008) 1009.
25. B.H. Lim, E.H. Majlan, W.R.W. Daud, M.I. Rosli and T. Husaini, *Int. J. Hydrogen Energy*, 42 (2017) 9210.
26. S.G. Kandlikar, Z. Lu, W.E. Domigan, A.D. White and M.W. Benedict, *Int. J. Heat Mass Transf.*, 52 (2009) 1741.
27. Z. Lu, S.G. Kandlikar, C. Rath, M. Grimm, W. Domigan, A.D. White, M. Hardbarger, J.P. Owejan and T.A. Trabold, *Int. J. Hydrogen Energy*, 34 (2009) 3445.
28. J. Wang and H. Wang, *Int. J. Hydrogen Energy*, 37 (2012) 10881.
29. S. Maharudrayya, S. Jayanti and A.P. Deshpande, *J. Power Sources*, 157 (2006) 358.
30. J. Ge, A. Higier and H. Liu, *J. Power Sources*, 159 (2006) 922.
31. E.U. Ubong, Z. Shi and X. Wang, *J. Electrochem. Soc.*, 156 (2009) B1276.
32. H.C. Liu, W.M. Yang, L.S. Cheng and J. Tan, *Fuel Cells*, 18 (2018) 173.
33. P. Quan and M.C. Lai, *J. Power Sources*, 164 (2007) 222.
34. P. Sun, *Comput. Methods Appl. Mech. Eng.*, 200 (2011) 3324.
35. Y.M. Ferng and A. Su, *Int. J. Hydrogen Energy*, 32 (2007) 4466.
36. L. Xing, X. Song, K. Scott, V. Pickert and W. Cao, *Int. J. Hydrogen Energy*, 38 (2013) 14295.